The
University
Of
Sheffield.

This is a repository copy of *Reverse glacier motion during iceberg calving and the cause of glacial earthquakes*.

White Rose Research Online URL for this paper:
http://eprints.whiterose.ac.uk/97243/

Version: Submitted Version

White Rose
university consortium
Universities of Leeds, Sheffield & York

eprints@whiterose.ac.uk
https://eprints.whiterose.ac.uk/

Title:

Reverse glacier motion during iceberg calving and the cause of glacial earthquakes

Authors:

T. Murray[1]*, M. Nettles[2], N. Selmes[1], L. M. Cathles[3], J. C. Burton[4], T. D. James[1], S. Edwards[5], I. Martin[5], T. O'Farrell[6], R. Aspey[6], I. Rutt[1], and T. Baugé[7]

Affiliations:

[1]Glaciology Group, Department of Geography, College of Science, Swansea University, Swansea SA2 8PP, UK

[2]Lamont-Doherty Earth Observatory, Columbia University, New York, NY 10964 USA

[3]Department of Atmospheric, Oceanic and Space Sciences, University of Michigan, Ann Arbor, MI 48109 USA

[4]Department of Physics, Emory University, Atlanta, GA 30322 USA

[5]School of Civil Engineering and Geosciences, Newcastle University, Newcastle upon Tyne, NE1 7RU, UK

[6]Department of Electronic and Electrical Engineering, University of Sheffield, Sheffield S1 3JD, UK

[7]Thales, Research & Technology, Worton Drive, Reading, Berkshire, RG2 0SB, UK

*Correspondence to: t.murray@swansea.ac.uk

Abstract:

Nearly half of Greenland's mass loss occurs through iceberg calving, but the physical mechanisms operating during calving are poorly known and *in situ* observations are sparse. We show that calving at Greenland's Helheim Glacier causes a minutes-long reversal of the glacier's horizontal flow and a downward deflection of its terminus. The reverse motion results from the horizontal force caused by iceberg capsize and acceleration away from the glacier front. The downward motion results from a hydrodynamic pressure drop behind the capsizing berg, which also causes an upward force on the solid Earth. These forces are the source of glacial earthquakes, globally detectable seismic events whose proper interpretation will allow remote sensing of calving processes occurring at an increasing number of outlet glaciers in Greenland and Antarctica.

Main Text:

One third to one half of Greenland's total mass loss occurs through iceberg calving at the margins of tidewater-terminating glaciers (*1, 2*). Recent, rapid changes in glacier dynamics are associated with increased calving rates (*3-5*) and increased rates of glacial earthquakes (*6*). At large glaciers with near-grounded termini, calving typically occurs when buoyancy forces cause icebergs the full thickness of the glacier to capsize against the calving front (*6-9*). This type of calving is associated with glacial earthquakes (*6, 7, 10*), long-period seismic emissions of magnitude ~5 that are observed globally (*11*). The earthquakes have expanded northward and increased seven-fold in number during the last two decades (*6, 12, 13*), tracking changes in glacier dynamics, the retreat of glacier fronts, and increased mass loss (*6, 14*). Buoyancy-driven calving represents an increasingly important source of dynamic mass loss (*6-8*) as glacier fronts throughout Greenland have retreated to positions near their grounding lines (*15*). However, due

58 to the difficulty of instrumenting the immediate near-terminus region of these highly active

59 glaciers, few direct observations of the calving process are available, limiting development of the

60 deterministic calving models required for improved understanding of controls on dynamic ice-

61 mass loss. Detailed knowledge of the glacial-earthquake source would allow quantification of

62 calving processes at a large class of Greenland glaciers as well as in several regions of Antarctica

63 (*13*).

64   Agreement on the source mechanism of glacial earthquakes is limited. Analysis of long-

65 period seismic data shows that a sub-horizontal force acts approximately perpendicular to the

66 glacier calving front during the earthquakes (*6, 13*). The observed seismic signal is generated

67 over a period of one minute or more (*6, 11, 16*), much longer than the source duration for

68 tectonic earthquakes of similar size (*17*). Some authors favor a model in which momentum

69 transfer produces a force acting in the upglacier and then downglacier directions as a newly

70 calved iceberg overturns, accelerates away from the calving front and subsequently decelerates

71 (*6, 10, 13*). Others suggest that the seismic signal arises from the iceberg scraping along the

72 calving front or fjord bottom (*7*) or colliding with the glacier terminus (*18*). Hydrodynamic

73 interactions with fjord water may be important (*19*) but are little explored. Analytical

74 investigations admit more than one possible mechanism for the earthquakes (*20*), and no

75 persuasive explanation has been presented for the vertical component of the earthquake force.

76 Here, we combine geodetic, seismic and laboratory data to identify the forces acting during

77 calving at large glaciers and document the source of the associated seismic signals.

78   We recorded geodetic data at the calving margin of Helheim Glacier (Fig. 1) (*9*), a major

79 outlet of the Greenland Ice Sheet, during 55 days in July-September 2013. A wireless network of

80 on-ice GPS sensors (*21*) captured glacier motion with cm-level accuracy at positions very close

81   to the calving front at a high temporal sampling rate (*22*). Hourly images from two cameras

82   located ~4 km down-fjord from and looking at the calving front were used in stereo

83   configuration to obtain the 3D geometry of the calving front and calved icebergs (*8, 22*). Data

84   from the global seismographic network were analysed for the same time period to identify glacial

85   earthquakes (*13, 23*) and obtain source parameters (*11*) including the orientation of the force

86   active during the earthquake, the earthquake centroid-single-force (CSF) amplitude, and the

87   earthquake centroid time, t_c (centroid of the temporal force history) (*22*).

88   The glacier retreated ~1.5 km in a series of calving events during the observing period.

89   We identified ten large calving events from the camera images. All coincided with glacial

90   earthquakes; in two cases, two earthquakes occurred between subsequent images. During the

91   earthquakes, the region near the calving front shows a dramatic reversal of flow, moving

92   upglacier for several minutes while simultaneously moving downward (Fig. 2, Fig. S1). The

93   horizontal and vertical motion then rebound rapidly.

94   Observations from a glacial earthquake occurring on Day of Year (DOY) 206 at 03:13:47

95   are shown in Figs. 2A and 2C. Analysis of camera images indicates ice loss of 0.461 ± 0.009 km^2

96   (Fig. 1) at a location of ice thickness 0.79 km, yielding an iceberg volume of 0.36 km^2 with

97   aspect ratio 0.23. The earthquake had CSF amplitude 0.24×10^{14} kg-m, with the force oriented

98   64°W (Fig. 1) and 9° above the horizontal. GPS sensor 1 (Fig. 1) showed a pre-earthquake flow

99   speed of 29 m/day. Immediately prior to the earthquake centroid time, the sensor reversed its

100   direction and moved upglacier at ~40 m/day (displacement 9 cm) and downward (displacement

101   10 cm). The reversed motion was sustained for ~200 seconds and was followed by a downglacier

102   rebound at ~190 m/day (displacement 20 cm) and upward movement (16 cm) for ~90 seconds.

103   Similar temporally coincident signals are seen on nearby sensors 6 and 15 (Fig. 1, Fig. S1).

104   Figures 2B and 2D show glacier deflection for a calving event on DOY 212 (Fig. 1). We

105   observe similar responses for all glacial-earthquake / calving events during which GPS sensors

106   recording data of adequate quality were located within 500 m of the calved block (a total of 9

107   glacial earthquakes and 8 image pairs). These events occurred on DOY 205, 206 (three events),

108   207, 211, 212, and 226 and are observed on multiple GPS sensors (further examples in Fig. S1).

109   The earthquake centroid times occur at or near the end of the glacier's rapid rebound

110   phase, such that the upglacier earthquake force aligns in time with the reverse motion of the

111   glacier. The horizontal glacier deflection is consistent with a model in which the reaction force

112   on the glacier due to seaward acceleration of the newly calved iceberg compresses the glacier

113   front elastically. The front then rebounds as the force decreases and reverses polarity during

114   iceberg deceleration. The glacier front thus acts as a spring, compressing and re-extending in

115   phase with the applied force, which is the horizontal component of the seismic source.

116   The downward deflection of the glacier front occurs in a region where vertical motion of

117   the GPS sensors at tidal frequencies shows the glacier is ungrounded and seawater is present

118   beneath it. Iceberg rotation is likely to cause a low-pressure zone in the opening cavity between

119   the iceberg and the glacier front. This pressure decrease would lower the load on the bedrock,

120   resulting in an upward force acting on the solid Earth, as observed in our seismic analysis. A

121   pressure decrease near the calving front would apply a net downward force on the glacier

122   terminus, lowering the glacier surface in a manner similar to that occurring twice each day when

123   the ocean tides draw down the water level. At sensors experiencing earthquake deflections, we

124   observe variations in vertical position due to the water tide of ~0.1 m per 1 m of tidal variation.

125   The calving-related deflection of the glacier surface is ~0.1-0.16 m, suggesting a change in water

126   pressure equivalent to a water-height change of ~1-1.6 m, or roughly 1-2 x 10^4 Pa.

127   No observations of pressure or water-level variations are available from the region in the

128   fjord immediately in front of the glacier, where thick ice mélange (Fig. 1) prohibits

129   instrumentation. However, results from analog laboratory experiments allow us to evaluate our

130   inferences (*22*). A model glacier "terminus" was secured at one end of a water-filled tank, and

131   plastic "icebergs" made from low-density polyethylene were placed flush against the terminus

132   and allowed to capsize spontaneously under the influence of gravitational and buoyancy forces

133   (*24*; Fig. 3). Sensors embedded in the model glacier terminus monitored pressure in the water

134   column and the force exerted on the terminus during iceberg capsize.

135   The measured force on the terminus as the iceberg begins to capsize is oriented in the

136   upglacier direction and slowly increases as the iceberg rotates. As the iceberg nears horizontal,

137   the force decreases rapidly. Pressure at the terminus decreases as the iceberg rotates, increasing

138   again as the iceberg nears horizontal. Once the iceberg loses contact with the terminus, the

139   measured force and pressure begin to oscillate due to induced wave action in the tank.

140   We scaled up the measured forces and pressures to match the dimensions of icebergs

141   calved at Helheim Glacier (Fig. 3). The laboratory data scale by powers of the ratio of the

142   iceberg height in the field to the iceberg height in the laboratory (*19,24*). The scaled peak force

143   agrees well with typical values inferred from earthquake analysis ($\sim 10^{11}$ N). The scaled peak

144   pressure drop ($\sim 5 \times 10^4$ Pa) applied over an area corresponding to the iceberg's map-view

145   dimensions yields an upward-directed force consistent with the seismically inferred vertical force

146   component, such that the total force acting on the solid Earth is oriented $\sim 10°$ above the

147   horizontal. Computation and inversion of synthetic seismograms from the scaled force and

148   pressure data confirms the consistency of the laboratory model with real-world data.

149   We use the scaled force and pressure to predict the deformation of the terminus region

150   (*22*). The total force F_{tot} per unit area A_F acting on the calving region produces a horizontal,

151   linear deflection orthogonal to the calving front $F_{tot}/A_F = E\Delta L/L$, where E is the Young's

152   modulus of glacial ice. The value of L is chosen to provide the best match to the glacier position

153   data. This length-scale likely represents the distance from the terminus to the grounding zone.

154   We model the ungrounded section of the glacier as an elastic beam of length L loaded by the

155   vertical force due to the pressure drop. The inferred distances L are a few km, consistent with

156   values estimated from GPS data.

157   Glacier displacements predicted from the scaled laboratory data for iceberg dimensions

158   corresponding to a calving event on DOY 206 (Fig. 1, Fig. 2A) are shown in Fig. 3. Agreement

159   with the observed glacier displacement is very good, particularly during the time over which the

160   force acts in the upglacier direction (until the earthquake centroid time). After this time, the

161   laboratory-derived prediction is dominated by oscillations of the water column in the tank, which

162   does not contain the thick layer of ice mélange present in Helheim Fjord and expected to damp

163   such high-frequency oscillations.

164   We conclude that as large icebergs rotate and accelerate away from the glacier calving

165   front (Fig. 4), the reaction force, which is the horizontal component of the earthquake force,

166   compresses the glacier front elastically, overcoming normal downglacier flow and temporarily

167   reversing the motion of the glacier. Hydrodynamic interaction of the iceberg with the fjord water

168   rapidly reduces pressure behind the rotating iceberg, resulting in an upward force on the solid

169   Earth that is the vertical force observed in the earthquake. The lowered water pressure draws

170   down the ungrounded glacier margin, pulling the glacier surface downward during the

171   earthquake.

172   Our results document the forces active during an increasingly important class of calving

173   events and definitively identify the processes that cause glacial earthquakes. This understanding

174   of glacier calving and glacial earthquakes opens the potential for remote, quantitative

175   characterisation of iceberg calving and calving rates, as well as improved models for ice-ocean

176   interaction.

177   **References and Notes:**

178   1. M. van den Broeke *et al.,* Partitioning recent Greenland mass loss. *Science* **326**, 984-986
179   (2009).

180   2. E. M. Enderlin *et al.,* An improved mass budget for the Greenland ice sheet. *Geophys. Res.*
181   *Lett.* **41**, 866-872 (2014).

182   3. I. Joughin, W. Abdalati, M. Fahnestock, Large fluctuations in speed on Greenland's
183   Jakobshavn Isbræ glacier. *Nature* **432**, 608-610 (2004).

184   4. A. Luckman, T. Murray, R. de Lange, E. Hanna, Rapid and synchronous ice-dynamic
185   changes in East Greenland. *Geophys. Res. Lett*. **33**, L03503 (2006).

186   5. I. M. Howat, I. Joughin, T. A. Scambos, Rapid changes in ice discharge from Greenland
187   outlet glaciers. *Science* **315**, 1559-1561 (2007).

188   6. S. A. Veitch, M. Nettles, Spatial and temporal variations in Greenland glacial-earthquake
189   activity, 1993-2010. *J. Geophys. Res.* **117**, F04007 (2012).

190   7. J. M. Amundson *et al.,* Glacier, fjord, and seismic response to recent large calving events,
191   Jakobshavn Isbrae, Greenland. *Geophys. Res. Lett.* **35**, L22501 (2008).

192   8. T. D. James, T. Murray, N. Selmes, K. Scharrer, M. E. O'Leary, Buoyant flexure and basal
193   crevassing in dynamic mass loss at Helheim Glacier. *Nature Geosci.* **7**, 593-596 (2014).

194   9. M. Nettles *et al.,* Step-wise changes in glacier flow speed coincide with calving and glacial
195   earthquakes at Helheim Glacier. Greenland. *Geophys. Res. Lett.* **35**, L24503 (2008).

196   10. G. Ekström, M. Nettles, G. A. Abers, Glacial earthquakes. *Science* **302**, 622-624 (2003).

197   11. G. Ekström, M. Nettles, V. C. Tsai, Seasonality and increasing frequency of Greenland
198   glacial earthquakes. *Science* **311**, 1756-1758 (2006).

199   12. M. Nettles, G. Ekström, Glacial earthquakes in Greenland and Antarctica. *Ann. Rev. Earth*
200   *Planet. Sci.* **38**, 467-491 (2010).

201   13. I. Joughin *et al.,* Ice-front variation and tidewater behavior on Helheim and Kangerdlugssuaq
202   Glaciers, Greenland. *J. Geophys. Res.*, **113,** F01004 (2008).

203   14. I. M. Howat, A. Eddy, Multi-decadal retreat of Greenland's marine-terminating glaciers. *J.*
204   *Glaciol.*, **57**, 389-396 (2011).

205   15. V. C. Tsai, G. Ekström, Analysis of glacial earthquakes. *J. Geophys. Res.* **112**, F03S22
206   (2007).

207 16. G. Ekström, E. R. Engdahl, Earthquake source parameters and stress distribution in the Adak
208   Island region of the central Aleutian Islands, Alaska. *J. Geophys. Res*. **94**, 15,499-15,519
209   (1989).

210 17. F. Walter *et al.,* Analysis of low-frequency seismic signals generated during a multiple-
211   iceberg calving event at Jakobshavn Isbræ, Greenland. *J. Geophys. Res*. **117**, F01036 (2012).

212 18. J. M. Amundson, J. C. Burton, S. Correa-Legisos, Impact of hydrodynamics on seismic
213   signals generated by iceberg collisions. *Ann. Glaciol.* **53**, 106–112 (2012).

214 19. V. C. Tsai, J. R. Rice, M. Fahnestock, Possible mechanisms for glacial earthquakes. *J.*
215   *Geophys. Res.* **113**, F03014 (2008).

216 20. I. Martin *et al.,* High-resolution sensor network for monitoring glacier dynamics. *IEEE*
217   *Sensors J.* **14**, 3926-3931 (2014).

218 21. Materials and methods are available as supplementary materials on *Science* Online.

219 22. G. Ekström, Global detection and location of seismic sources by using surface waves. *Bull.*
220   *Seism. Soc. Am*. **96**, 1201-1212 (2006).

221 23. J. C. Burton *et al.,* Laboratory investigations of iceberg capsize dynamics, energy dissipation
222   and tsunamigenesis. *J. Geophys. Res.* **117**, F01007 (2012).

223 24. H. Kawakatsu, Centroid single force inversion of seismic waves generated by landslides. *J.*
224   *Geophys. Res.* **94**, 12363-12374 (1989).

225 25. A. M. Dziewonski, D. L. Anderson, Preliminary reference Earth model. *Phys. Earth Planet.*
226   *Inter*. **25**, 297-356 (1981).

227 26. T. D. James, T. Murray, N. E. Barrand, S. L. Barr, Extracting photogrammetric ground
228   control from lidar DEMs for change detection. *Photogramm. Rec.* **21,** 310-326 (2006).

229 27. C. Leuschen, C. Allen, IceBridge MCoRDS L3 Gridded Ice Thickness, Surface, and Bottom,
230   Version 2, Helheim_2008_2012_Composite. Boulder, Colorado USA: NASA DAAC at the
231   National Snow and Ice Data Center. http://nsidc.org/data/irmcr3.html (2013).

232 28. J. F. Zumberge, M. B. Heflin, D. C. Jefferson, M. M. Watkins, F. H. Webb, Precise point
233   positioning for the efficient and robust analysis of GPS data from large networks. *J.*
234   *Geophys. Res.* **102**, 5005-5017 (1997).

235 29. J. Saastamoinen, Contributions to the theory of atmospheric refraction. *Bull. Geodesique* **107**,
236   13-34 (1973).

237 30. J. Boehm, A. Niell, P. Tregoning, H. Schuh, Global Mapping Function (GMF): A new
238   empirical mapping function based on numerical weather model data. *Geophys. Res. Lett.* **33**,
239   L07304 (2006).

240 31. F. Lyard, F. Lefevre, T. Letellier, O. Francis, Modelling the global ocean tides: modern
241   insights from FES2004. *Ocean Dynamics* **56**, 394-415 (2006).

242 32. IERS Conventions (2010). G. Petit and B. Luzum (eds.). (IERS Technical Note ; 36)
243   Frankfurt am Main: Verlag des Bundesamts für Kartographie und Geodäsie,. 179 pp. (2010).

244 33. W. Bertiger *et al*., Single receiver phase ambiguity resolution with GPS data. *J. Geod.* **84**,
245   327-337 (2010).

246   34. G. Chen, GPS kinematic positioning for the airborne laser altimetry at Long Valley,
247   California. Ph.D. thesis, Mass. Inst. of Technol., Cambridge (1998).

248   35. R. Dach *et al.,* GNSS processing at CODE: status report. *J. Geod.* **83**, 353-365 (2009).

249   36. J. C. Burton, L. M. Cathles, W. G. Wilder, The role of cooperative iceberg capsize in ice-
250   shelf disintegration. *Annals Glaciol.* **54**, 84-90 (2013).

251   37. I. H. Cho, M. H. Kim, Wave absorbing system using inclined perforated plates. *J. Fluid*
252   *Mech.* **606**, 1-20 (2008).

253   38. D. R. MacAyeal, D. S. Abbot, O. V. Sergienko, Iceberg-capsize tsunamigenesis. *Annals*
254   *Glaciol.* **52**, 51-56 (2011).

255   39. D. G. Vaughan, Tidal flexure at ice shelf margins. *J. Geophys. Res.* **100**, 6213-6224 (1995).

256   40. E. Rignot, Tidal motion, ice velocity and melt rate at Petermann Gletscher, Greenland,
257   measured from radar interferometry. *J. Glaciol.* **42**, 476-485 (1996).

273 **Supplementary Materials:**

274 Materials and Methods

275 Figure S1

276 References (*25-41*)
277
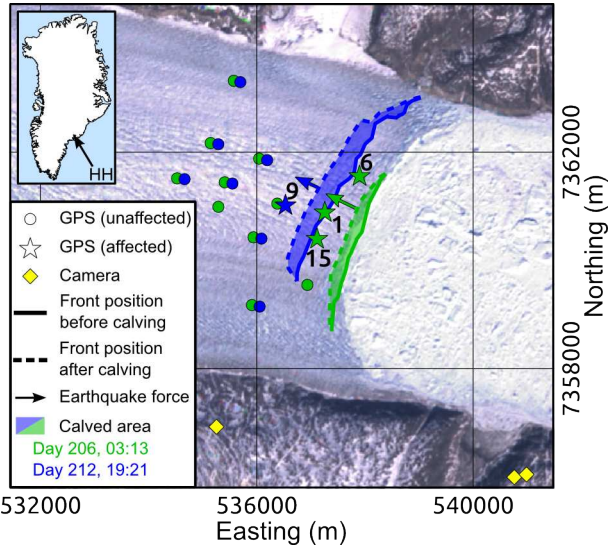
Fig. 1. Helheim Glacier, position of sensors, and seismic force directions. Location of GPS sensors and icebergs calved at Helheim Glacier (HH) for glacial-earthquake events at 03:13 DOY 206 2013 and 19:21 DOY 212 2013, superimposed on Landsat 7 image from DOY 167 2013. 'Affected' sensors exhibit earthquake-related deflections. Scan-line-corrector failure stripes have been removed for clarity. Glacier flow from left to right; bright white mélange (mix of iceberg fragments and sea ice) can be seen in front of calving margin. Calving-front positions obtained from photogrammetric DEMs derived from cameras. Times are UTC, positions are meters UTM zone 24N.
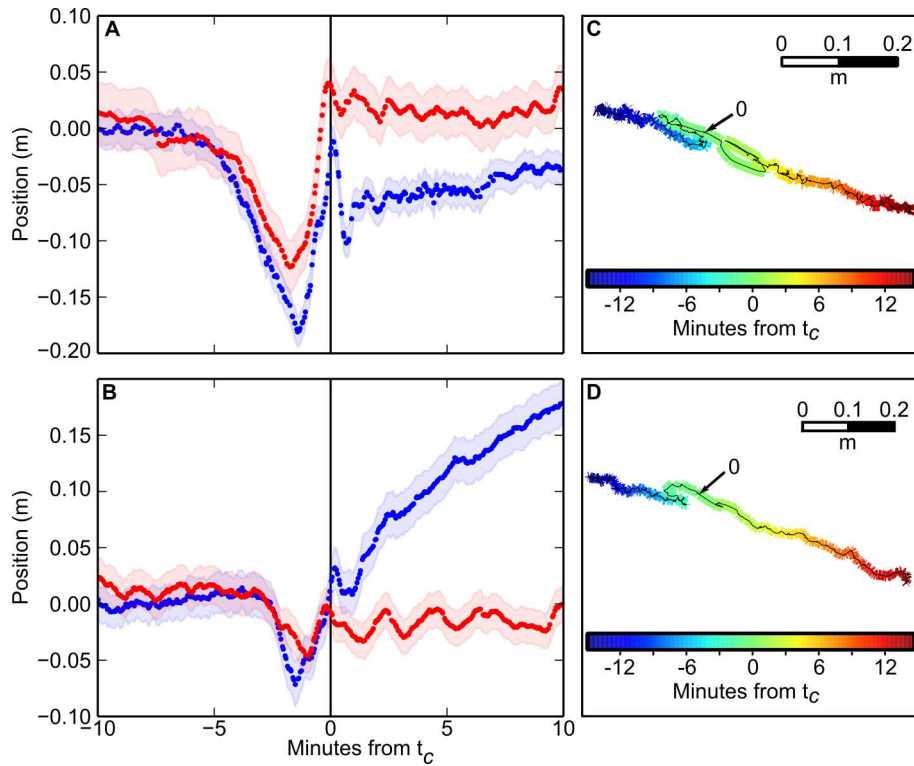
Fig. 2. Response of GPS sensors on glacier at the time of glacial earthquakes. (A) Sensor 1 at 03:13 on DOY 206 2013. (B) Sensor 9 at 19:21 on DOY 212 2013. Blue dots show detrended along-flow displacement, red dots show height. Shading shows 1σ position errors. Earthquake centroid time t_c. Horizontal displacement has trend from 30-10 mins before t_c removed (A=28.9 m/day, B=24.6 m/day). Height has mean removed. (C) and (D) Plan view of GPS traces shown in (A) and (B) during 30 minutes around t_c, marked as 0.
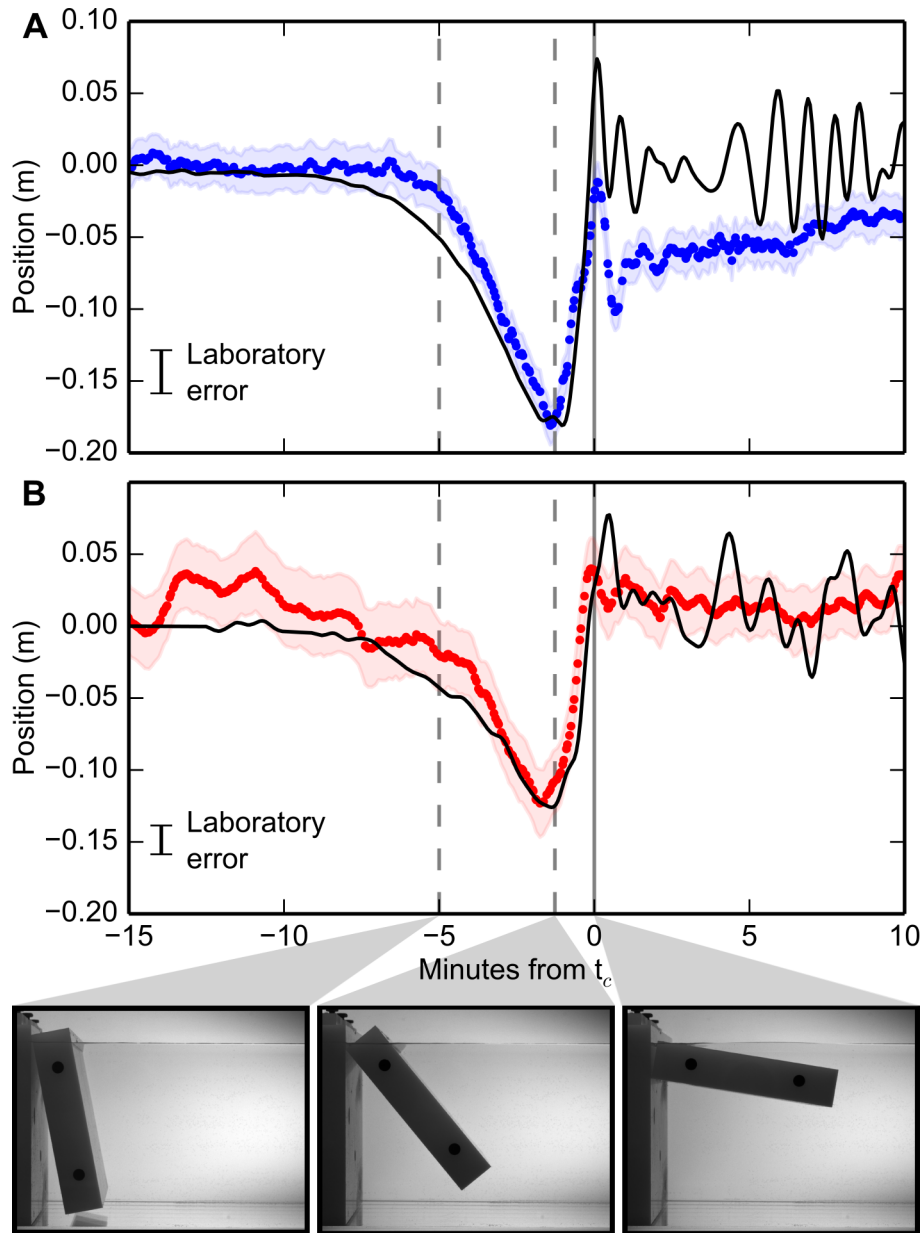
Fig. 3. Scaled laboratory data from glacier "terminus" during "iceberg" capsize event compared to field observations. (A) Horizontal displacement scaled from force (black line) compared to downflow GPS data (blue). (B) Vertical displacement scaled from pressure (black line) compared to vertical GPS data (red). Errors in laboratory data are standard deviation from repeated capsize events. GPS data as in Figure 2A. Photographs show stage of capsize at times marked by dashed lines and (solid gray line) t_c. Aspect ratio of model iceberg is 0.22.

304
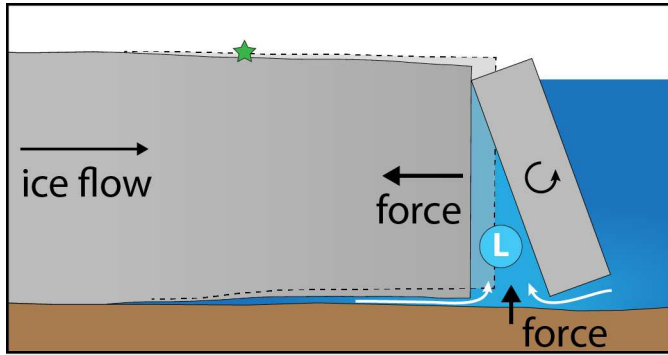
Fig. 4. Cartoon of glacier terminus during calving event. Glacier deflection caused by
capsizing iceberg shown relative to initial position (dotted line). Acceleration of iceberg to right
exerts a force in the upglacier direction (left), leading to reverse motion of the GPS sensors
(green star). Reduced pressure behind the iceberg ("L") draws water from beneath the glacier
and from the proglacial fjord, pulling the floating portion of the glacier downward and exerting
an upward force on the solid Earth.